



# Nearly zero peroxydisulfate consumption for persistent aqueous organic pollutants degradation via nonradical processes supported by in-situ sulfate radical regeneration in defective MIL-88B(Fe)

Yu-Hang Li <sup>a,b</sup>, Chong-Chen Wang <sup>a,b,\*</sup>, Fei Wang <sup>a,b</sup>, Wen Liu <sup>c</sup>, Long Chen <sup>c</sup>, Chen Zhao <sup>a,b</sup>, Huifen Fu <sup>a,b</sup>, Peng Wang <sup>a,b</sup>, Xiaoguang Duan <sup>d,\*\*</sup>

<sup>a</sup> Beijing Key Laboratory of Functional Materials for Building Structure and Environment Remediation, School of Environment and Energy Engineering, Beijing University of Civil Engineering and Architecture, Beijing 100044, China

<sup>b</sup> Beijing Energy Conservation & Sustainable Urban and Rural Development Provincial and Ministry Co-construction Collaboration Innovation Center, Beijing University of Civil Engineering and Architecture, Beijing 100044, China

<sup>c</sup> College of Environmental Sciences and Engineering, Peking University, The Key Laboratory of Water and Sediment Sciences, Ministry of Education, Beijing 100871, China

<sup>d</sup> School of Chemical Engineering, The University of Adelaide, Adelaide, South Australia 5005, Australia



## ARTICLE INFO

### Keywords:

Defective MIL-88B(Fe)  
Persulfate regeneration  
Nonradical Pathway  
Persistent bisphenol A degradation

## ABSTRACT

The porous defective MIL-88B(Fe) with abundant oxygen vacancies and Fe-N sites was fabricated to accomplish nearly zero peroxydisulfate (PDS) consumption for persistent bisphenol A (BPA) degradation via electron-transfer pathway (ETP). Interestingly, the generated sulfates during ETP were oxidized to yield the confined sulfate radicals and to accomplish the peroxydisulfate regeneration in the fine-tuned MIL-88B(Fe), which was verified by series experiments and DFT calculations. Further studies suggested that the optimal De-MIL-88B(Fe)-1.25 catalyst achieved the persistent nonradical reactions for BPA decomposition under visible light irradiation with both low input and low consumption of PDS. It was the first case to achieve nearly zero PDS consumption for emerging pollutants elimination, which provided new strategy to design and tune defective metal-organic frameworks for the purpose of reducing the stoichiometry between PDS and contaminants for nearly zero PDS consumption.

## 1. Introduction

Recently, the persulfate-based nonradical oxidation processes (PS-NOPs) involving singlet oxygen ( ${}^1\text{O}_2$ ), electron-transfer pathway (ETP) and high-valent metals, had been extensively explored to eliminate emerging organic contaminants from wastewater matrix [1–4]. PS-NOPs displayed more advantages than radicals-based advanced oxidation processes (AOPs) in actual wastewater treatment because of the high selectivity toward electron-rich contaminants, high efficiency in a wide pH working window, and free of toxic intermediates [5–7]. Among them, one crucial advantage was typically neglected that nonradical pathways could accomplish high chemical utilization efficiency due to the low stoichiometry between persulfate and contaminants, which

remarkably reduced the persulfate input and was more economical than conventional AOPs [8]. In typical ETP regime, electron-rich organic substances contributed electrons to surface-activated persulfate via the catalyst shuttle to generate  $\text{SO}_4^{2-}$ . Moreover, previous study reported that metal-based catalyst displayed enough positive valence band potential, which was capable of oxidizing  $\text{SO}_4^{2-}$  to generate  $\text{SO}_4^{\bullet-}$  at sufficiently high  $E_{\text{VB}}$  condition [9,10]. Therefore, it was essential to design a metal-based catalyst with high  $E_{\text{VB}}$  to oxidize the as-produced  $\text{SO}_4^{2-}$  during ETP to generate surface limited radicals ( $\text{SO}_4^{\bullet-}$ ), which enhanced the possibility of radical self-quenching reaction ( $\text{SO}_4^{\bullet-} + \text{SO}_4^{2-} \rightarrow \text{S}_2\text{O}_8^{2-}$ ,  $k = 4.0 \times 10^8 \text{ M}^{-1} \text{ s}^{-1}$ ) to yield persulfate for further achieving persistent nonradical reactions to degrade target contaminants.

Metal-organic frameworks (MOFs), as porous crystalline materials,

\* Corresponding author at: Beijing Key Laboratory of Functional Materials for Building Structure and Environment Remediation, School of Environment and Energy Engineering, Beijing University of Civil Engineering and Architecture, Beijing 100044, China.

\*\* Corresponding author.

E-mail addresses: [wangchongchen@bucea.edu.cn](mailto:wangchongchen@bucea.edu.cn) (C.-C. Wang), [xiaoguang.duan@adelaide.edu.au](mailto:xiaoguang.duan@adelaide.edu.au) (X. Duan).

were constructed from metal ions/metal-oxygen clusters and organic linkers, which were deemed as ideal catalysts due to the structural flexibility and surface chemistry [11–14]. The monocarboxylate ligands with functional groups containing nitrogen atom could be adopted as modulators to modulate the structure/composition of MOF via defect engineering, which could generate hierarchically porous structures, oxygen vacancies and extra electron-rich nitrogen sites [15,16]. The formation of oxygen vacancies and nitrogen sites inside the framework were expected to accelerate ETP [17,18]. Also, the hierarchically porous structures promoted PDS adsorption via strengthening mass transfer rate to accelerate ETP. Meanwhile, such porous structures provided more sorption sites to confine the as-produced  $\text{SO}_4^{2-}$  and  $\text{SO}_4^{\bullet-}$ , further facilitating to regenerate peroxydisulfate (PDS) for ongoing oxidation process.

To address the above critical points, a facile fabrication strategy was firstly presented via adding 4-aminonicotinic acid with different concentrations into the precursor solution of MIL-88B(Fe) to obtain defective MIL-88B(Fe) (De-MIL-88B(Fe)-X, De represented defect engineering, and X represented the molar ratio of 4-aminonicotinic acid/benzene-1,4-dicarboxylic acid). PDS was selected as the persulfate activator, considering that the symmetry structure of PDS was favorable for the regeneration. Meanwhile, the low-spin PDS@catalyst complexes could be easily formed to promote ETP upon metal-based catalyst interacting with the strong-field persulfate (PDS) [19]. In this work, quantitative structure-activity relationships (QSARs) confirmed that such hierarchically porous catalysts with increasing rich oxygen vacancies and Fe-N sites contents accelerated the ETP during the bisphenol A (BPA) degradation. Integrated with radical scavenging tests, electron paramagnetic resonance (EPR), in-situ Raman, electrochemical methods and density functional theory (DFT) calculations, we revealed that the electron-transfer process was the major BPA degradation pathway. In addition, defective MIL-88B(Fe) possessed more positive valence band potential than pristine MIL-88B(Fe), which could in-situ oxidize the produced sulfate during ETP to generate surface-confined  $\text{SO}_4^{\bullet-}$ , further achieving the regeneration of PDS. DFT calculations were further performed to affirm that the formed oxygen vacancies and Fe-N sites in the framework of defective MIL-88B(Fe) effectively dumbed down the obstacle of transformation from  $\text{SO}_4^{2-}$  to  $\text{S}_2\text{O}_8^{2-}$ . Among all the as-prepared De-MIL-88B(Fe)-X, De-MIL-88B(Fe)-1.25, as the optimal catalyst, displayed outstanding BPA degradation performance via PDS activation under visible light irradiation. More interestingly, compared to MIL-88B(Fe), De-MIL-88B(Fe)-1.25 could realize persistent elimination toward BPA due to the ultra-low consumption of PDS. In addition, the total PDS consumption for effective BPA degradation was ultra-low during the five-cycle experiments in the De-MIL-88B(Fe)-1.25/PDS/light system. To our best knowledge, no reports were available on tuning the structure/composition of catalysts to reduce the stoichiometry between persulfate and contaminants. As the first case of reducing the consumption of persulfate, this work provided new insight into the rational design of MOFs for persulfate-oriented nonradical oxidation for the purpose of rapid and continuous decontamination of aqueous micropollutants.

## 2. Materials and methods

### 2.1. Chemicals

Iron(III) chloride hexahydrate ( $\text{FeCl}_3 \cdot 6\text{H}_2\text{O}$ ), benzene-1,4-dicarboxylic acid ( $\text{H}_2\text{BDC}$ ), 4-aminonicotinic acid, sodium hydroxide ( $\text{NaOH}$ ), sodium persulfate (PDS,  $\text{Na}_2\text{S}_2\text{O}_8$ ), benzoic acid (BA), 4-Hydroxybenzoic Acid (HBA), bisphenol A (BPA), atrazine (ATZ), humic acid (HA), deuterium oxide ( $\text{D}_2\text{O}$ ), isopropyl alcohol (IPA) and furfuryl alcohol (FFA) were brought from J&K company. Methyl phenyl sulfoxide (PMSO), methyl phenyl sulfone (PMSO<sub>2</sub>) and potassium iodide (KI) were purchased from MACKUNIN company. Dimethylformamide (DMF) and ethanol (EtOH) were obtained from Tianjin Fu Chen

Chemical Co., Ltd. (China). Ethylene diamine tetraacetic acid (EDTA),  $\text{KClO}_4$ ,  $\text{NaCl}$ ,  $\text{NaHCO}_3$ ,  $\text{NaH}_2\text{PO}_4$  and  $\text{Na}_2\text{SO}_4$  were brought from Sino-pharm Chemical Reagent Co., Ltd. (China).

### 2.2. Synthesis of catalysts

The MIL-88B(Fe) powder was synthesized by a modified method [20]. Particularly, the solutions of 0.5 mmol  $\text{FeCl}_3 \cdot 6\text{H}_2\text{O}$  (40.0 mg) and 0.5 mmol benzene-1,4-dicarboxylic acid (28.5 mg) dissolved in 5.0 mL  $\text{N,N}$ -dimethylformamide (DMF). Then, 0.4 mL  $\text{NaOH}$  aqueous solution with the concentration of 4.0 M was added to the mixed solution. The mixed solution was transferred into a 25.0 mL Teflon lined autoclave, followed by heating at 100 °C for 12.0 h. The fabrication method of De-MIL-88B(Fe)-X was similar with that of MIL-88B(Fe), except that the 4-aminonicotinic acid with different dosages was introduced into the precursor solution of MIL-88B(Fe) during the fabrication process. The number “X” represented the molar ratio of 4-aminonicotinic acid/ $\text{H}_2\text{BDC}$ . Then, the as-prepared powder was washed with alcohol three times and dried at 60.0 °C for 12.0 h.

### 2.3. Characterizations

The physicochemical properties of the as-prepared catalysts were characterized by the scanning electron microscope (SEM), high resolution transmission electron microscopy (HR-TEM), powder X-ray diffraction (PXRD), Fourier transform infrared spectra (FTIR), X-ray photoelectron spectra (XPS), X-ray absorption spectroscopy (XAS), UV-Vis diffuse reflectance spectra (UV-Vis DRS), Brunauer-Emmett-Teller (BET), elemental analyses (EA) and electron paramagnetic resonance (EPR). The detailed information of the characterization techniques and DFT calculations were presented in [Supporting Information \(SI, Section S1\)](#).

### 2.4. Catalytic experiments and analyses

To evaluate the degradation performance, 20.0 mg of the catalyst was added to 50.0 mL BPA solution (10.0 mg  $\text{L}^{-1}$ ) and stirred for 30.0 min to reach the adsorption-desorption equilibrium in the dark. The degradation experiment was initiated by the addition of PDS under the irradiation of 300 mW low-power LED visible light (PCX50C, Beijing Perfectlight Technology Co., Ltd). During the degradation process, 1.0 mL solution was filtrated by using a 0.22  $\mu\text{m}$  PTFE membrane from the reactor every 10.0 min. 20.0  $\mu\text{L}$  methanol was added into the filtrate to terminate the oxidation reaction. The residual BPA concentrations would be determined by ultra-high performance liquid chromatography (UHPLC, Thermo Scientific Vanquish Flex). The detection methods of targeted pollutants and detection of ROSSs were described in [SI, Section S2](#).

### 2.5. Analysis of PDS concentration

Iodometric spectrophotometry was selected to detect the concentration of the residual PDS [21,22]. 10.0  $\mu\text{L}$  filtrate was mixed with 10.0 mL KI solution (2.4 M), and the mixed solution was stirred for 10.0 min to ensure the reaction between PDS and  $\text{I}^-$  to generate the yellow-colored  $\text{I}_3^-$  ([Eqs. S2 and S3](#)). The  $\text{I}_3^-$  concentration, proportional to PDS, was determined at  $\lambda_{\text{max}} = 352\text{ nm}$  by UV-vis spectrophotometer.

### 2.6. Cyclivity experiments

20.0 mg catalyst was added into a 50.0 mL BPA solution (10.0 mg  $\text{L}^{-1}$ ), and the mixed solution was stirred for 30.0 min in the dark. Under the irradiation of visible light, 1.0 or 6.0 mM PDS solution was added into the BPA solution. After oxidation for 60.0 min, 2.5 mL solution was filtrated to determine residual BPA and PDS concentration. Then, only 2.5 mL BPA stock solution (200.0 mg  $\text{L}^{-1}$ ) was added into the reactor to

carry out the next cyclic experiment.

### 3. Results and discussion

#### 3.1. Characterizations

The synthesis procedures of pristine MIL-88B(Fe) and series De-MIL-88B(Fe)-X were illustrated in Fig. 1a (synthesis details could be seen in Supporting Information). The amount of 4-aminonicotinic acid in De-MIL-88B(Fe)-X were 0.1, 0.2, 0.3 and 0.4 mmol, respectively. As shown in the SEM and HR-TEM images (Fig. 1b, c, S1b–d and S2a–d), the morphologies of the as-prepared catalysts changed from nanorods (MIL-88B(Fe)) to spindles (De-MIL-88B(Fe)-1.25) as the dosage of 4-aminonicotinic acid gradually increased to 0.4 mmol. The alteration of preferred crystal facets may be attributed to the coordination of 4-aminonicotinic acid. The corresponding HR-TEM elemental mapping (Fig. 1d–h and S2e–h) exhibited that the uniform distribution of N element from 4-aminonicotinic acid throughout De-MIL-88B(Fe)-1.25. The PXRD patterns (Fig. S1a) revealed that the exposed degree of crystal facet (101) of the engineered De-MIL-88B(Fe)-X was weaker than that of pristine MIL-88B(Fe). In addition, the intensities of characteristic

peaks at  $2\theta = 13.12^\circ$  and  $16.02^\circ$  of De-MIL-88B(Fe)-X gradually turned stronger with the increasing 4-aminonicotinic acid content. The exposed crystal facet (101) might display better persulfate activation performance than that of crystal facet (002) [23], implying that the persulfate activation ability to generate radicals would decline with the increasing 4-aminonicotinic acid content in De-MIL-88B(Fe)-X.

DFT calculations were performed to construct the optimal models of De-MIL-88B(Fe)-X, and to determine the possibility of coordination between N from 4-aminonicotinic acid and Fe-O cluster. As displayed in Fig. 2a, the formation energy values of various structures were negative, indicating that Fe-O cluster could theoretically coordinate with both pyridine N and amino N. The FTIR spectra (Fig. S3) demonstrated that two new peaks at  $433\text{ cm}^{-1}$  and  $680\text{ cm}^{-1}$  appeared in De-MIL-88B(Fe)-X, which were contributed to the bonding interactions between pyridine and Fe-O clusters, respectively [24]. The XPS N 1 s spectrum (Fig. S4c) showed that the red shifts of 0.55 eV and 0.45 eV accordingly occurred to pyridine N and amino N of De-MIL-88B(Fe)-1.25 compared to 4-aminonicotinic acid, indicating that pyridine N and amino N were probably coordinated with Fe on the Fe-O cluster. In the characteristic Fe 2p peaks (Fig. S4b), the decreased peak area ratio of Fe-O-C (BDC) (ca. 724.9 and 711.4 eV [20,25]) in the total peak areas demonstrated that the content

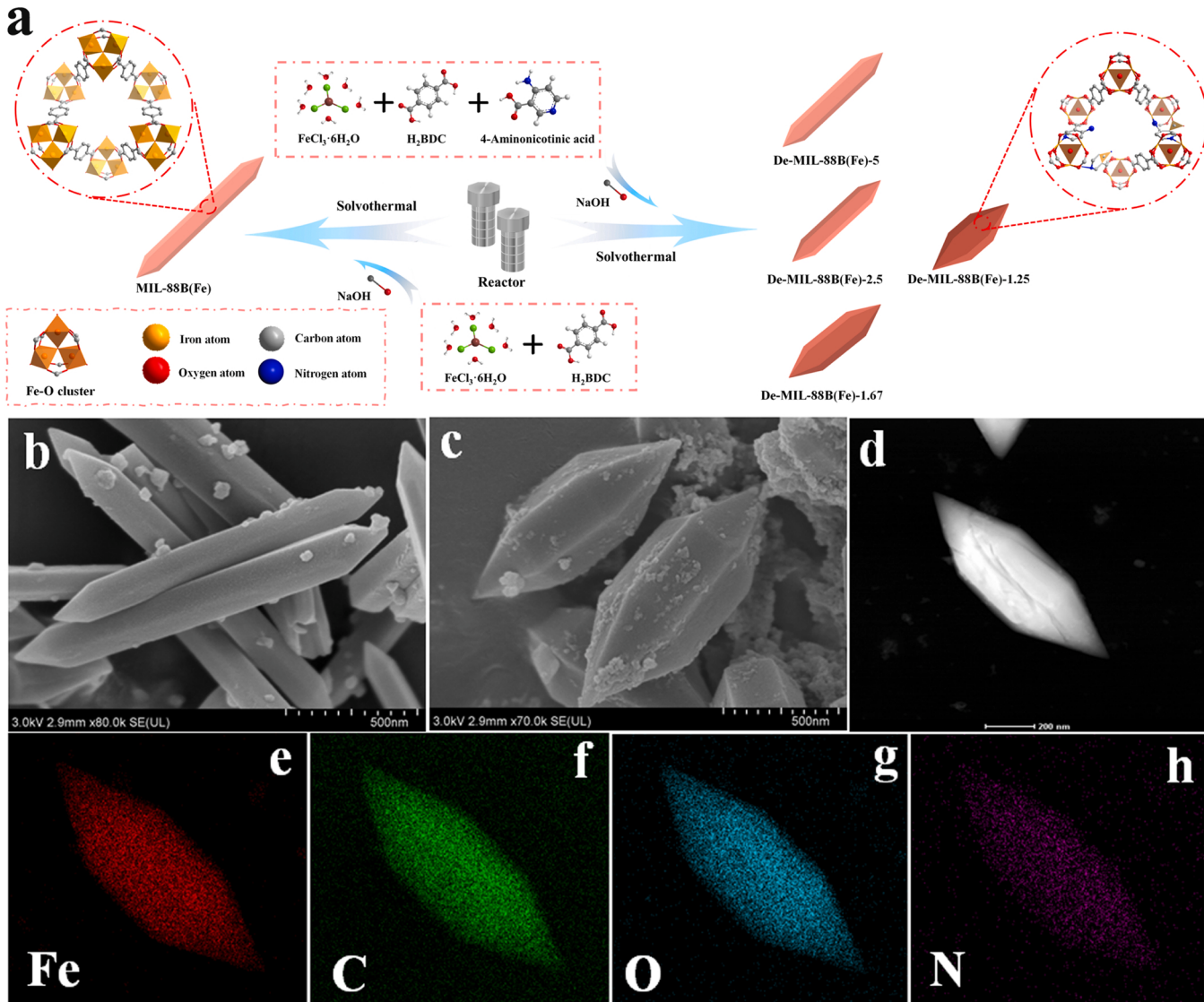
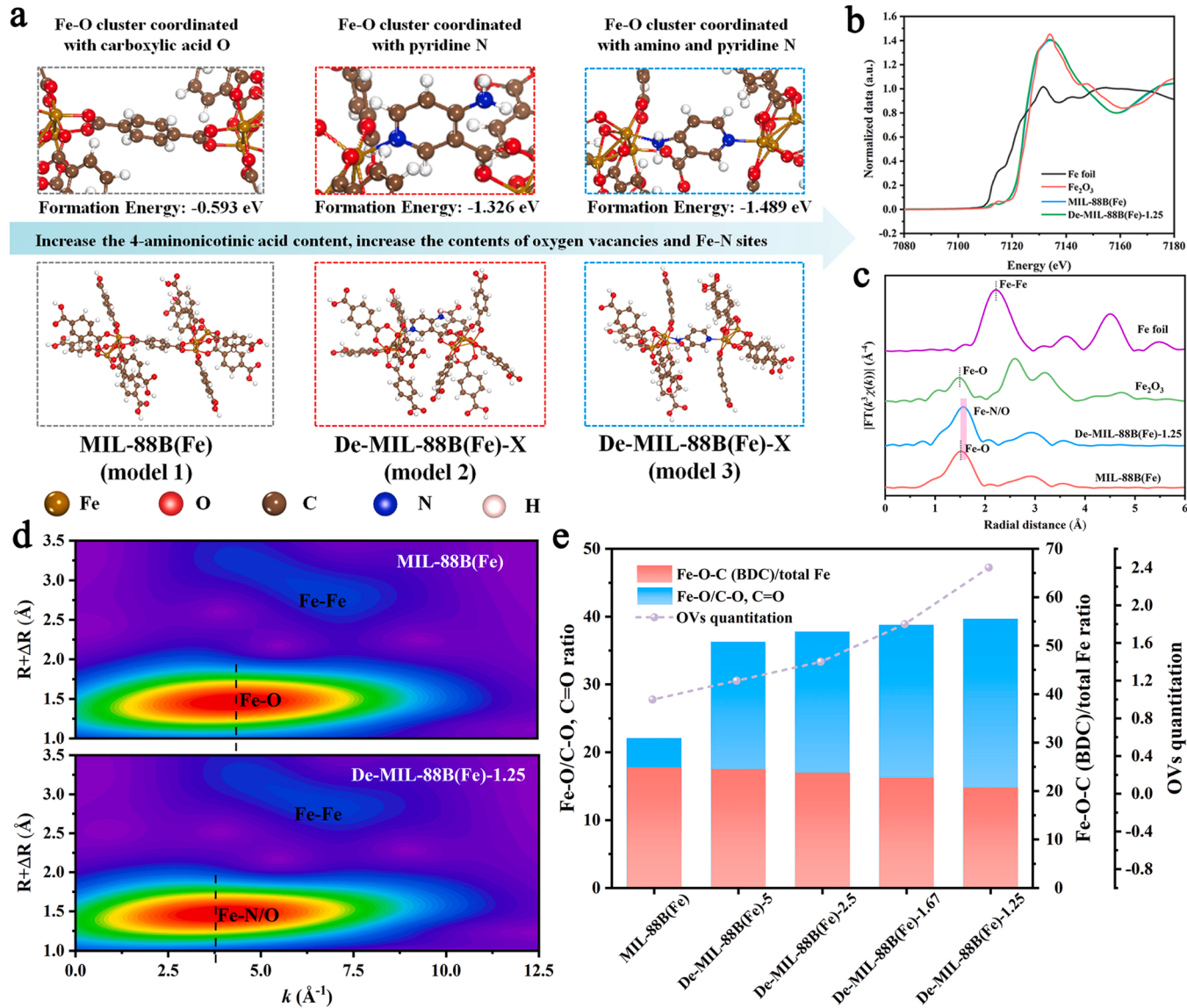


Fig. 1. The schematic illustration for (a) pristine MIL-88B(Fe) and series De-MIL-88B(Fe)-X. The SEM images of (b) MIL-88B(Fe) and (c) De-MIL-88B(Fe)-1.25. (d–h) HR-TEM image of De-MIL-88B(Fe)-1.25 and its corresponding element mapping.



**Fig. 2.** (a) The DFT calculated formation energies of MIL-88B(Fe) and De-MIL-88B(Fe)-X (b) XANES and (c) EXAFS spectra of the Fe K-edge in MIL-88B(Fe) and De-MIL-88B(Fe)-1.25. (d) WT plot of the Fe K-edge EXAFS for MIL-88B(Fe) and De-MIL-88B(Fe)-1.25. (e) The Fe-O/C-O, C=O ratio, Fe-O-C (BDC)/total Fe ratio and OVs quantitation.

of Fe-N increased with the introduced 4-aminonicotinic acid content (Fig. 2e). The Fe K-edge XANES spectra (Fig. 2b and Table S1) of De-MIL-88B(Fe)-1.25 displayed that the absorption edge position was located between the Fe foil and  $\text{Fe}_2\text{O}_3$ , indicating that the average positive charge on the Fe atoms was between + 2 and + 3. The EXAFS spectra (Fig. 2c) illustrated that De-MIL-88B(Fe)-1.25 exhibited a strong peak at 1.56  $\text{\AA}$ , which was different from the pristine MIL-88B(Fe) (1.51  $\text{\AA}$ ). The change of average bond distance was attributed to the formation of Fe-N bonds [26]. From the results of wavelet transformed (WT) Fe K-edge EXAFS oscillations (Fig. 2d and S5), an obvious blue shift of  $0.6 \text{ \AA}^{-1}$  happened to De-MIL-88B(Fe)-1.25 compared to MIL-88B(Fe), implying the formation of Fe-N in the framework of De-MIL-88B(Fe)-1.25. The EXAFS fitting results of both MIL-88B(Fe) and De-MIL-88B(Fe)-1.25 in R space demonstrated that the average coordination number of Fe was close to 5.0 (Fig. S6 and Table S1), implying that unsaturated coordination sites might exist in the framework as the ideally saturated coordination number of Fe is 6.0. The EPR quantitation spectra (Fig. S4d) of both pristine MIL-88B(Fe) and De-MIL-88B(Fe)-X displayed a peak at  $g = 2.004$  (oxygen vacancy) with increasing intensity [27], which might be attributed to the growing amount of

uncoordinated sites with the increased 4-aminonicotinic acid content (Fig. 2e, Table S2). The characteristic O 1 s peaks (Fig. S4a) of all catalysts at 532.33, 531.6 and 531.1 eV affirmed the presence of C-O, C=O and Fe-O bonds [28,29], respectively. The increasing density of oxygen vacancies could be attributed to the decreasing in C-O and C=O, and the increasing peak area ratio of Fe-O/C-O (or C=O) indicated a higher content of oxygen vacancies in De-MIL-88B(Fe)-X than MIL-88B(Fe) (Fig. 2e).

As depicted in Fig. S7 and Table S3, all De-MIL-88B(Fe)-X rather than the pristine MIL-88B(Fe) possessed extra mesopores (8.0–36.0 nm), providing abundant space to adsorb and activate PDS by the exposed Fe-N sites and oxygen vacancies via strengthening the mass transfer rates. All catalysts could absorb the visible light based on the UV-vis DRS spectra (Fig. S8a). The band gaps (Fig. S8b) of MIL-88B(Fe) and series De-MIL-88B(Fe)-X were calculated via Eq. (S4) to be 2.95 eV, 2.90 eV, 2.83 eV, 2.76 eV and 2.80 eV, respectively [30,31].

### 3.2. Persulfate activation for catalytic degradation

PDS activation activities of various catalysts were evaluated by

removing bisphenol A (BPA) under the low-power LED visible light irradiation (300 mW). Firstly, the BPA removal efficiency via the adsorption process over De-MIL-88B(Fe)-1.25 (Fig. S9a) was maintained at around 52.84% without PDS and light, indicating that the complete BPA removal was attributed to the catalytic degradation rather than individual adsorption. The cyclic experiments (Fig. S9b) demonstrated that the sorption capacity of both MIL-88B(Fe) and De-MIL-88B(Fe)-1.25 remained in a specific range (about 40.0%–50.0%) in dark during six cycles. The BPA degradation efficiency of De-MIL-88B(Fe)-1.25 could still achieve over 99.0% even in the 6th cyclic experiment. Additionally, the adsorbed BPA onto De-MIL-88B(Fe)-1.25 after adsorption-desorption equilibrium was calculated to be 13.193 mg g<sup>-1</sup>. After catalytic degradation, the residual BPA on the De-MIL-88B(Fe)-1.25 was 0.01225 mg g<sup>-1</sup>, indicating that more than 99.9% BPA adsorbed on the De-MIL-88B(Fe)-1.25 could be degraded via the catalytic process. As shown in Fig. 3a and S10, the catalytic BPA degradation efficiencies and rates of all De-MIL-88B(Fe)-X were better than pristine MIL-88B(Fe) in the presence of both light and PDS. The Fe-N sites and oxygen vacancies might play dominant roles in PDS activation [32–34]. The results of established QSARs exhibited (Fig. 3b) that the degradation rate was accelerated with the increased contents of oxygen vacancies (Eq. 1) and Fe-N sites (Eq. 2). The De-MIL-88B(Fe)-1.25 with the maximum densities of oxygen vacancies and Fe-N was selected as the optimal catalyst to achieve the best BPA degradation efficiency (over 99.0%) and the biggest rate constant ( $k_{\text{obs}}$  was 0.04898 min<sup>-1</sup>). In addition, 14.68% of total organic carbon (TOC) could be eliminated in De-MIL-88B(Fe)-1.25/light/PDS system. The results of BPA degradation pathways (Figs. S11–S13) and toxicity analyses (Fig. S14) of the generated intermediates demonstrated that De-MIL-88B(Fe)-1.25/PDS/light system displayed better detoxification effect than that of MIL-88B(Fe)/PDS/light system.

$$\ln k_{\text{obs}} = 1.01(\pm 0.032)C_{\text{OVS}} - 5.48(\pm 0.05) R^2 = 0.997 \quad (1)$$

$$\ln k_{\text{obs}} = 1.72(\pm 0.086)C_{\text{Fe-N}} - 11.29(\pm 0.37) R^2 = 0.996 \quad (2)$$

Figs. S15 and S16 demonstrated that BPA degradation was relied on the light irradiation in De-MIL-88B(Fe)-1.25/light/PDS system, as the introduction of visible light might reduce the resistance of catalyst to further facilitate charge transfer [35]. The BPA removal efficiencies did not present obvious variation when the PDS concentrations were gradually increased from 1.0 mM to 8.0 mM in De-MIL-88B(Fe)-1.25/PDS/light system, indicating that the ETP rather than reactive oxygen species (ROSSs) might be the dominant motivation for BPA degradation (Fig. S17). De-MIL-88B(Fe)-1.25 could exhibit the satisfactory degradation efficiency over a wide initial solution pH range (3.03–7.94) (Fig. 3c and S18). As shown in Fig. 3d, H<sub>2</sub>PO<sub>4</sub><sup>-</sup> retarded BPA degradation partly, while the influences of Na<sup>+</sup>, K<sup>+</sup>, Ca<sup>2+</sup>, Cl<sup>-</sup>, SO<sub>4</sub><sup>2-</sup> and humic acid (HA) were negligible. As it was known, H<sub>2</sub>PO<sub>4</sub><sup>-</sup> might produce a relatively strong affinity toward the surface of the catalyst or yield complexes with the iron sites [36,37], further inhibiting the BPA degradation. In addition, the intervention of HA (a hole scavenger) was negligible in De-MIL-88B(Fe)-1.25/light/PDS system, indicating that photo-induced hole oxidation of BPA could be ignored [38]. Fig. 3e and Table S4 displayed the abundant inorganic ions and organic matters were existed in both tap water and lake water. Fig. 3f exhibited that De-MIL-88B(Fe)-1.25 could display satisfactory degradation efficiencies in different simulated wastewater containing BPA formulated by drinking water, tap water and lake water, demonstrating its outstanding practical application prospects.

### 3.3. Analyses of active species

The contribution of radical oxidation toward BPA degradation over De-MIL-88B(Fe)-1.25 was excluded by series control experiments. As shown in Fig. S9a, BPA was hard to be degraded in PDS/light system, indicating that it was difficult to achieve efficient BPA elimination

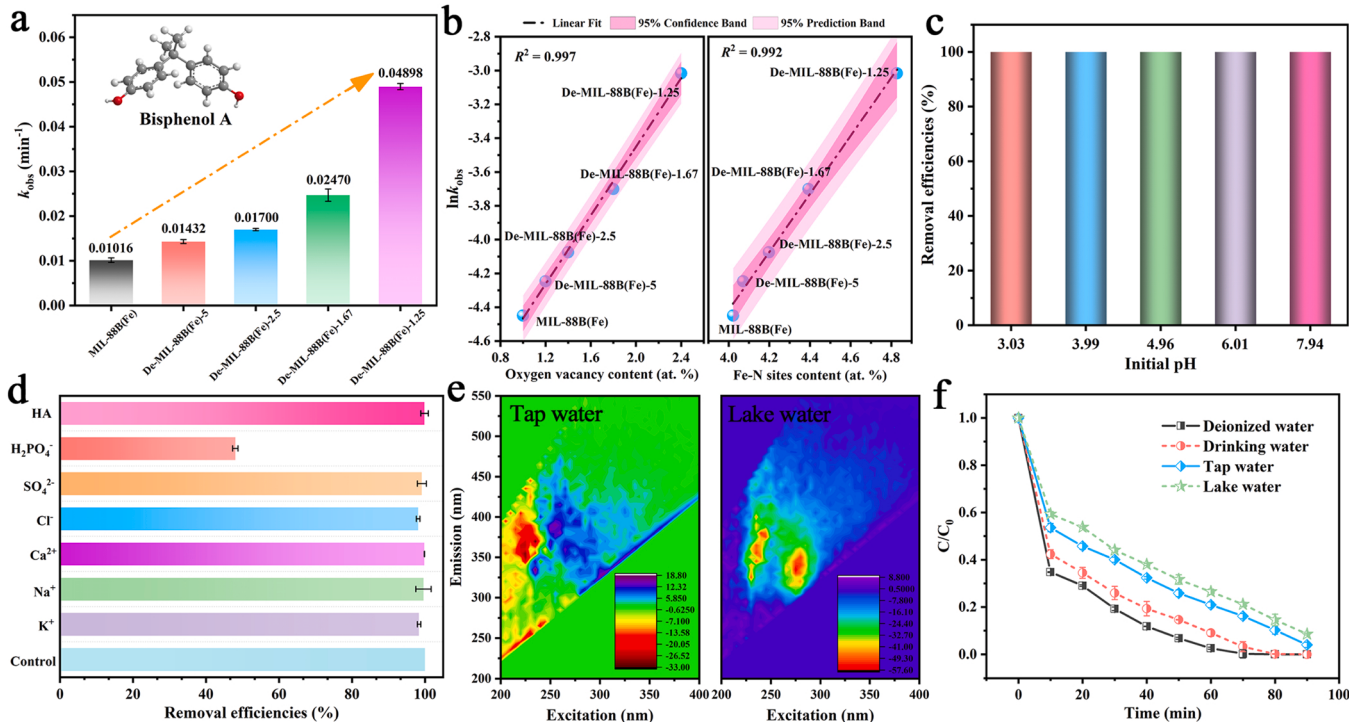


**Fig. 3.** (a) The BPA degradation reaction rate constants over different catalysts under visible light. Reaction conditions: catalysts = 400.0 mg L<sup>-1</sup>, BPA = 10.0 mg L<sup>-1</sup>, volume = 50.0 mL, PDS = 2.0 mM, pH = 6.01. (b) The influences of oxygen vacancy and Fe-N sites content on reaction rates over MIL-88B(Fe) and series De-MIL-88B(Fe)-X. (c) The influences of initial pH values on BPA removal efficiencies over De-MIL-88B(Fe)-1.25. (d) Influences of inorganic ions and organic matter on BPA degradation efficiencies over De-MIL-88B(Fe)-1.25. (e) The emission-excitation matrix spectra of tap water and lake water. (f) The BPA degradation efficiencies of De-MIL-88B(Fe)-1.25 in different simulated wastewater.

without the aid of De-MIL-88B(Fe)-1.25 catalyst. In addition, the dissolved  $\text{Fe}^{2+}$  or  $\text{Fe}^{3+}$  with low-concentration (1.0 mg  $\text{L}^{-1}$ ) provided slight influence toward BPA degradation in the presence of both PDS and light (Fig. S19), in which the concentration of iron ion dissolved from De-MIL-88B(Fe)-1.25 was determined by ICP-OES. In dark, the BPA removal efficiency in De-MIL-88B(Fe)-1.25/PDS system was similar to De-MIL-88B(Fe)-1.25, indicating that the material cannot directly activate PDS without the irradiation of visible light. De-MIL-88B(Fe)-1.25 could be activated to generate photo-induced  $\text{e}^-$  and  $\text{h}^+$  under visible light irradiation, in which the formed hydrated electrons ( $\text{e}_{\text{aq}}$ ) could be captured by TEMPO in EPR determination [39]. It was observed that the signal intensity of TEMPO- $\text{e}_{\text{aq}}$  (1:1:1,  $A_N = 17.3$  G) was weaker than that of TEMPO (Fig. S20), indirectly demonstrating the presence of photo-induced  $\text{h}^+$  in De-MIL-88B(Fe)-1.25/light/PDS system. The results of EPR test (Fig. S21a) indicated that the signals of both DMPO- $\text{SO}_4^{2-}$  ( $A_N = 13.8$  G,  $A_H = 10.1$  G) and DMPO- $\bullet\text{OH}$  ( $A_N = A_H = 14.9$  G) could be observed, indicating the generation of  $\text{SO}_4^{2-}$  and  $\bullet\text{OH}$  in the MIL-88B(Fe)/light/PDS system. However, only the signal of DMPO- $\bullet\text{OH}$  was observed, meaning that PDS was difficult to be excited to produce  $\text{SO}_4^{2-}$  in De-MIL-88B(Fe)-1.25/light/PDS system. As well, the generation of  $\bullet\text{OH}$  was attributed to the reaction between photo-induced  $\text{h}^+$  and  $\text{OH}^-/\text{H}_2\text{O}$ . The results of quantitative determination of  $\bullet\text{OH}$  and  $\text{SO}_4^{2-}$  were consistent with the results of EPR test (Fig. S22). The contribution of radicals ( $\text{SO}_4^{2-}$  and  $\bullet\text{OH}$ ) in the system could be evaluated via determining the ATZ degradation efficiency. Fig. S21b displayed that the oxidation efficiency of MIL-88B(Fe) toward ATZ ( $k_{\text{ATZ}} = 3.0 \times 10^9 \text{ M}^{-1} \text{ s}^{-1}$ ,  $k_{\bullet\text{OH}} = 3.0 \times 10^9 \text{ M}^{-1} \text{ s}^{-1}$ ) [40] was better than that of De-MIL-88B(Fe)-1.25 in 60.0 min, preliminarily confirming that radicals ( $\text{SO}_4^{2-}$  and  $\bullet\text{OH}$ ) presented a weak contribution in De-MIL-88B(Fe)-1.25/light/PDS system. To further evaluate the contribution of radicals, ethanol (MeOH) and isopropyl alcohol (IPA) were used to scavenge radicals due to their high affinity towards free radicals. The BPA degradation efficiencies (Fig. S23a and b) in MIL-88B(Fe)/light/PDS system slowed down with the increased concentration of MeOH (150 mM, 300 mM and 600 mM) or IPA (150 mM, 250 mM and 500 mM). The quenching results implied the critical role of free radicals in the MIL-88B(Fe)/light/PDS system. By contrast, Fig. S23c and d showed that the inhibiting effects of MeOH or IPA at different concentrations were ignored in the De-MIL-88B(Fe)-1.25/light/PDS system. The above results might indicate that De-MIL-88B(Fe)-1.25/light/PDS oxidize BPA via a nonradical-mediated process. The results of EPR technique (Fig. S24a and c),  $\text{D}_2\text{O}$  experiment (Fig. S24b) and scavenger experiments (Figs. S24d and S25) indicated that the  $^1\text{O}_2$  formed from the transformation of  $\bullet\text{OH}$  made insignificant contribution toward BPA degradation [41–43]. Moreover, PMSO was selected to affirm metastable high-valence metal intermediates (Fe(VI)) during PDS activation [44]. Fig. S26 showed that the signal of PMSO<sub>2</sub> was very insignificant, indicating free of high-valent Fe-intermediates in the De-MIL-88B(Fe)-1.25/light/PDS system.

### 3.4. Probing the electron-transfer processes in nonradical process

It had been suggested that organic compounds with ionization potential (IP) lower than 9.0 eV may act as electron donors in ETP oxidation [45]. Herein, the IP value of BPA was  $\sim 7.5$ , which could serve as an electron donor [45]. If De-MIL-88B(Fe)-1.25 could mediate electron transfer between BPA and PDS, PDS was difficult to be directly activated without the presence of BPA. Conversely, if De-MIL-88B(Fe)-1.25 could directly activate PDS to generate ROSs, the pre-mixing of De-MIL-88B(Fe)-1.25 and PDS in advance would present a profound influence on the subsequent BPA removal due to the consumption of PDS and the limited lifetimes of ROSs. As shown in Fig. S27, an insignificant influence for BPA removal efficiencies with the increase of pre-mixing time indicated that PDS could not be activated directly by De-MIL-88B(Fe)-1.25, preliminarily showing that ETP might be the major oxidation process toward BPA degradation in the De-MIL-88B

(Fe)-1.25/light/PDS system. In addition, the previous study reported that the positive linear relationships should be presented between PDS adsorption quantity ( $Q_{\text{PDS}}$ ) and  $\ln k_{\text{obs}}$  if ETP was the main degradation pathway [8]. As shown in Fig. 4a and S28, the well-fitted (Eq. 3) and positive linear relationships of  $Q_{\text{PDS}}$  and  $\ln k_{\text{obs}}$  of different catalysts indicated that the larger PDS adsorption quantity offered faster electron transfer from BPA to the co-existing PDS over the catalyst surface, confirming the electron-transfer oxidation. Furthermore, DFT calculations revealed that the demanded adsorption energies between PDS and active sites of De-MIL-88B(Fe)-X were less than that of MIL-88B(Fe) (Fig. 4b), indicating that De-MIL-88B(Fe)-X with increasing oxygen vacancies and Fe-N sites contents could accelerate ETP for the enhanced BPA degradation. As well, the ethylenediaminetetraacetic acid (EDTA) as a complexing reagent was used to hinder the Fe sites [46]. Fig. 4c showed that the degradation efficiencies of BPA dramatically decreased when EDTA with different concentrations (5 mM and 10 mM) were added, indicating that Fe-N sites were the significant active sites for PDS activation. The formation of such reactive intermediate would capture electrons from the electron donor (in this case, BPA), leading to PDS activation for BPA oxidation. Moreover, the current-time chronoamperometric response (Fig. 4d) at 0.8 V demonstrated that a negative signal and a positive current signal were observed with the addition of PDS (electron acceptor) at 300 s and BPA (electron supplier) at 600 s, respectively. The negative signal revealed that PDS was adsorbed and co-existed on the surface of catalyst. When the BPA was added, the positive signal demonstrated the direction of electron transfer from electron supplier to the PDS co-existing over the catalyst surface, confirming the electron-transfer oxidation [19,47]. By contrast, when the PDS and BPA were added, respectively, the intensities of signal response were obviously weaker than those of De-MIL-88B(Fe)-1.25 system, demonstrating that the contribution of electron transfer pathway (ETP) was minor in individual MIL-88B(Fe) system (Fig. S29). In situ Raman measurement was performed to probe the surface chemical evolution during PDS activation [48]. As shown in Fig. 4e and f, a new peak ( $\text{S}_2\text{O}_8^{2-,*}$ ) appeared at around  $807 \text{ cm}^{-1}$  when De-MIL-88B(Fe)-1.25 was contacted with PDS, beside the pristine peak of  $\text{S}_2\text{O}_8^{2-}$  at around  $837 \text{ cm}^{-1}$ . This new peak could be attributed to the bending vibrations of the prolonged peroxy O-O bond in the De-MIL-88B(Fe)-1.25-PDS\* complexes [32]. In addition, the electron-transfer process over De-MIL-88B(Fe)-1.25-PDS\* complex gave rise to outer-sphere reactions with BPA, which could be affirmed by the inhibition of BPA degradation after the addition of  $\text{KClO}_4$  with different concentrations (50 mM and 100 mM) (Fig. S30) [49]. Typically, with the increase of solution ionic strength, formed bonds (electrostatic bonding) via outer-sphere interactions will be broken due to the decrease of zeta potential of the catalyst surface. Therefore, the outer-sphere interaction was more sensitive to the variation of ionic strength than inner-sphere interactions [19], which was in good agreement with results of co-existing foreign matters experiments.

$$\ln k_{\text{obs}} = 0.99(\pm 0.003)Q_{\text{PDS}} - 4.63(\pm 0.03) R^2 = 0.996 \quad (3)$$

In situ Raman spectra (Fig. 4e and f) revealed that the new peak ( $\text{S}_2\text{O}_8^{2-,*}$ ) was still maintained after the addition of BPA, while the peak of  $\text{SO}_4^{2-}$  around  $982 \text{ cm}^{-1}$  never appeared, suggesting that PDS was not largely consumed during the oxidation. To verify the above conclusion, the BPA elimination efficiencies and residual PDS concentrations toward De-MIL-88B(Fe)-1.25/light/PDS system during the catalytic process were monitored. As shown in Fig. S31, the residual PDS concentrations at each time were nearly equal to the initial concentration. Furthermore, the PDS consumption was monitored for MIL-88B(Fe) and De-MIL-88B(Fe)-X, in which PDS consumption decreased with the increase in oxygen vacancies and Fe-N sites. De-MIL-88B(Fe)-1.25 exhibited the potential to achieve ultra-low and even near zero PDS consumption for continuous BPA elimination. The PDS consumptions over MIL-88B(Fe) and series De-MIL-88B(Fe)-X were tested in five cycle experiments, in

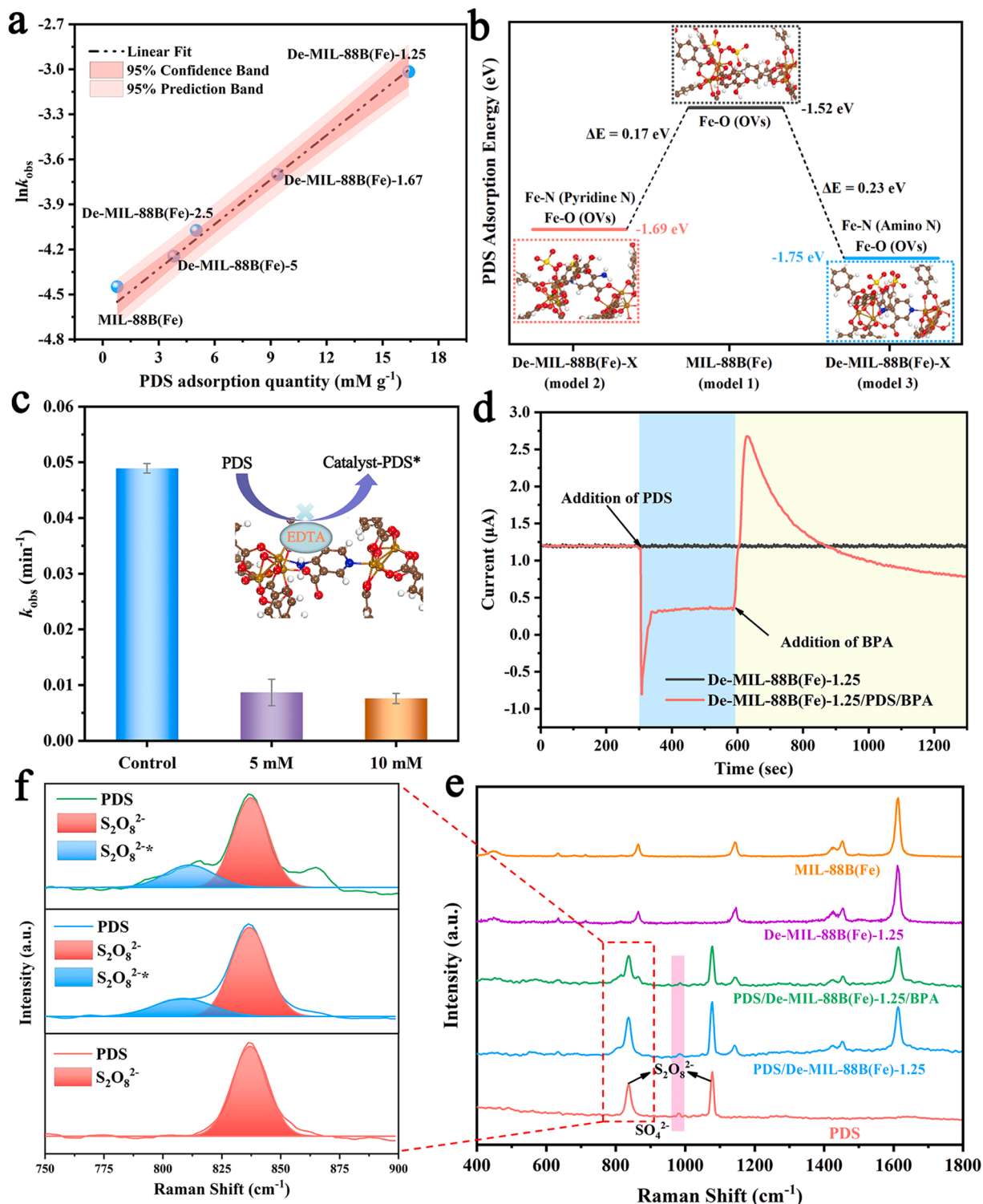


**Fig. 4.** (a) The correlation between  $\ln k_{\text{obs}}$  and PDS adsorption quantity. (b) The calculated PDS adsorption energy in different models. (c) The influences of EDTA with different concentrations on BPA elimination in De-MIL-88B(Fe)-1.25/PDS/light system (d) the charge migration during the activation of PDS and oxidation of BPA in De-MIL-88B(Fe)-1.25 system. (e) In-situ Raman spectra of PDS, PDS/De-MIL-88B(Fe)-1.25, PDS/De-MIL-88B(Fe)-1.25/BPA, MIL-88B(Fe) and De-MIL-88B(Fe)-1.25 in the aqueous solution (f) the magnified Raman spectra to highlight the generation of  $\text{S}_2\text{O}_8^{2-*}$ .

which 2.5 mL BPA solution with the concentration of  $200.0 \text{ mg L}^{-1}$  was added into the reactor to carry out the next cyclic experiment. As shown in Fig. 5a and b, De-MIL-88B(Fe)-1.25 still displayed near 100% BPA degradation efficiency, and the concentration of involved PDS remained nearly unchanged after five cycles. The good stability of De-MIL-88B(Fe)-1.25 was confirmed by SEM (Fig. S32a), PXRD (Fig. S32b), FTIR

(Fig. S32c), Fe dissolution (Fig. S32d) and XPS determination (Fig. S33). Furthermore, the cyclic performances and PDS consumption of other catalysts presented two rules: (i) the oxidation capacity was boosted with the increasing contents of oxygen vacancies and Fe-N sites; (ii) the consumptions of PDS would decrease with the increase of the content of oxygen vacancies and Fe-N sites during the degradation.

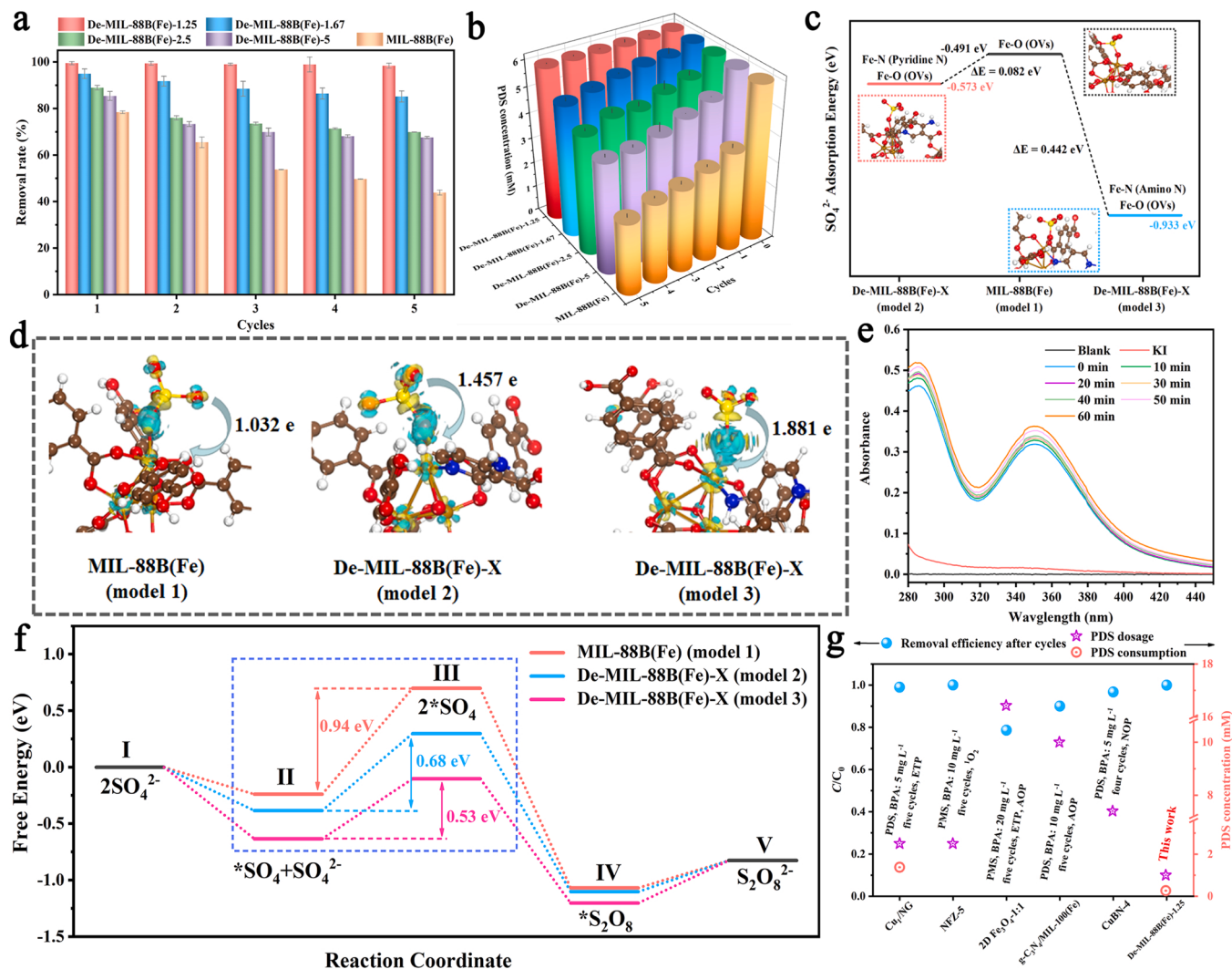


**Fig. 5.** (a) The cyclic performances of BPA removal over series catalysts and (b) their corresponding PDS residual concentrations. Experiments conditions: sorbent dose = 400.0 mg L<sup>-1</sup>, BPA = 10.0 mg L<sup>-1</sup>, PDS dosage in the first cyclic experiment = 6.0 mM. (c) The calculated  $\text{SO}_4^{2-}$  adsorption energy in different models. (d) Electron density difference of  $\text{SO}_4^{2-}$  adsorption in different models and their corresponding charge transfer. Blue and yellow electronic cloud density represented electron dissipation and accumulation, respectively. (e) The UV absorption spectra of the iodometric persulfate measurement system. Reaction conditions: De-MIL-88B(Fe)-1.25 = 400.0 mg L<sup>-1</sup>,  $\text{Na}_2\text{SO}_4$  = 6.0 mM, PDS = 6.0 mM, volume = 50.0 mL, pH = 6.01. (f) The reaction pathways of  $\text{S}_2\text{O}_8^{2-}$  regeneration in different models. (g) The comparison of cyclic performance, PDS dosage and PDS consumption of different catalysts toward BPA degradation [32,37,53–55].

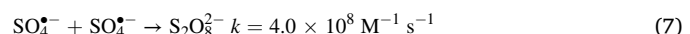
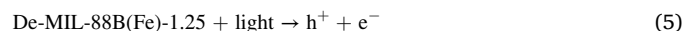
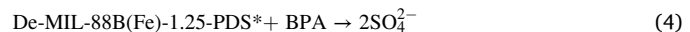
### 3.5. The mechanisms of PDS regeneration

The ultra-low PDS consumption was mainly attributed to the character of low stoichiometry of nonradical pathway and the regeneration of PDS. The formed De-MIL-88B(Fe)-1.25-PDS\* complex captured electrons from BPA to generate surface confined  $\text{SO}_4^{2-}$  (Eq. 4), which was confirmed by DFT calculations. Fig. 5c showed that  $\text{SO}_4^{2-}$  adsorbed on Fe-N sites of De-MIL-88B(Fe)-X were more energy favorable than that with Fe-O sites of MIL-88B(Fe), illustrating that generated  $\text{SO}_4^{2-}$  could be confined on the surface of De-MIL-88B(Fe)-1.25. Subsequently, the generated  $\text{SO}_4^{2-}$  could be oxidized to surface confined  $\text{SO}_4^{2-}$  by photo-induced  $\text{h}^+$  due to its high oxidation potential. The results of Mott-Schottky curves (Fig. S34) and UV-vis DRS spectrum (Fig. S8b) verified that the photo-generated holes (e.g., the HOMO of De-MIL-88B(Fe)-1.25 was 2.65 eV) could react with  $\text{SO}_4^{2-}$  to form  $\text{SO}_4^{2-}$  ( $\text{SO}_4^{2-}$ : 2.5–3.1 eV, Eqs. 5 and 6) [9]. Based on the adsorption energy calculation models for  $\text{SO}_4^{2-}$  sorption, differential charge density calculations (Fig. 5d) were performed to determine the corresponding charge transfer. Interestingly, the electrons transfer number from  $\text{SO}_4^{2-}$  to Fe-N sites on model 2 and model 3 were 1.457 eV and 1.881 eV, respectively,

which were much higher than that on Fe-O sites (1.032 eV) of model 1. The increased charge transfer could result in that  $\text{SO}_4^{2-}$  adsorbed on Fe-N sites preferred to lose electron to generate  $\text{SO}_4^{2-}$ . As expected, the generation of DMPO- $\text{SO}_4^{2-}$  (Fig. S35) indicated that photo-generated holes with the oxidizing capacities could accomplish the conversion of  $\text{SO}_4^{2-}$  to  $\text{SO}_4^{2-}$  in the De-MIL-88B(Fe)-1.25/light/PDS system. The adjacent surface confined  $\text{SO}_4^{2-}$  collided to regenerate  $\text{S}_2\text{O}_8^{2-}$  as Eq. (7). To verify above conclusion, the  $\text{SO}_4^{2-}$  ( $\text{Na}_2\text{SO}_4$ ) with the concentration of 6.0 mM was added into De-MIL-88B(Fe)-1.25/light/PDS system to estimate the concentration of  $\text{S}_2\text{O}_8^{2-}$  by iodometric spectrophotometry, further confirming whether  $\text{SO}_4^{2-}$  could be converted to  $\text{S}_2\text{O}_8^{2-}$ . As demonstrated in Fig. 5e, the enhanced intensity of absorbance of  $\text{I}_3^-$  indicated the increased concentration of  $\text{S}_2\text{O}_8^{2-}$ , meaning that  $\text{SO}_4^{2-}$  could be converted to  $\text{S}_2\text{O}_8^{2-}$ . Meanwhile, the previous studies reported that  $\text{H}_2\text{O}_2$  could be generated by photocatalytic reaction, in which  $\text{H}_2\text{O}_2$  could also oxidize  $\text{I}_2$  to generate  $\text{I}_3^-$  [50,51]. The Fig. S36 indicated that  $\text{I}_3^-$  was difficult to be produced in De-MIL-88B(Fe)-1.25/light system, eliminating the influence of self-produced  $\text{H}_2\text{O}_2$  on above results. Meanwhile, the extra  $\text{SO}_4^{2-}$  with different concentrations (400.0, 600.0 and 800.0 mg L<sup>-1</sup>) were added into De-MIL-88B(Fe)-1.25/light/PDS system

to monitor the concentration of  $\text{S}_2\text{O}_8^{2-}$ . As illustrated in Fig. S37, it was observed that 0.28 mM  $\text{S}_2\text{O}_8^{2-}$  could be produced when the concentration of additional  $\text{SO}_4^{2-}$  increased to 800.0 mg L<sup>-1</sup>, in which the final PDS concentration was the sum of the measured concentration and the concentration of PDS adsorbed onto the catalyst (Fig. S28). The generated persulfate heavily relied on the adsorption capacity of De-MIL-88B(Fe)-1.25 toward  $\text{SO}_4^{2-}$  and the number of active sites, rather than the introduced sulfate. Furthermore, the PDS concentration after cyclic experiments (Fig. 5b) was primarily constant with minor range of fluctuations, affirming the existence of  $\text{S}_2\text{O}_8^{2-}$  regeneration process in De-MIL-88B(Fe)-1.25/light/PDS system.

DFT calculations were further carried out to probe the insights of  $\text{S}_2\text{O}_8^{2-}$  regeneration mechanism on active sites of De-MIL-88B(Fe)-1.25. The produced intermediates of regeneration process and their corresponding Gibbs free energy ( $\Delta G$ ) profiles were exhibited in Fig. 5f and S38, in which model 1 along with model 2 and model 3 represented the Fe-O sites of MIL-88B(Fe) and the Fe-N sites of De-MIL-88B(Fe)-1.25. Firstly,  $2\text{SO}_4^{2-}$  (I) in the solution could be adsorbed on active sites to form  $^*\text{SO}_4 + \text{SO}_4^{2-}$  intermediate (II) with the release of energy. Importantly, the generation of 2  $^*\text{SO}_4$  intermediate (III) was the rate-limiting step toward three models. Fortunately, the desorption energy in model 2 (0.68 eV) and model 3 (0.53 eV) were much less than that of model 1 (0.94 eV). For De-MIL-88B(Fe)-1.25, the formation ability of 2  $^*\text{SO}_4$  intermediate was boosted via accelerating the rate-limiting step, further facilitating the formation of  $^*\text{S}_2\text{O}_8$  (IV). However, the released process of  $^*\text{S}_2\text{O}_8$  (V) as uns spontaneous one required more energies in model 2 and model 3 than that of model 1, which was in favor to accelerate ETP for BPA degradation. The above results indicated that the PDS could be reproduced via the transform from  $\text{SO}_4^{2-}$  to  $\text{SO}_4^{2-}$  and sulfate radical self-quenching reaction, leading to the ultra-low consumption during the BPA elimination process in De-MIL-88B(Fe)-1.25/light/PDS system.



### 3.6. Mechanism of nonradical involved in De-MIL-88B(Fe)-1.25/light/PDS system

Based on the above results, the mechanism of nonradical involved in the De-MIL-88B(Fe)-1.25/light/PDS system was proposed for BPA degradation (Fig. 6). Firstly, PDS was adsorbed onto the oxygen vacancies and Fe-N sites of De-MIL-88B(Fe)-1.25 and then was excited to generate a metastable De-MIL-88B(Fe)-1.25-PDS\* complex. The intermediates with a high redox state can drive electrons flow from co-adsorbed BPA via outer-sphere reaction to achieve BPA decomposition into lower-potential products [52], which was major degradation process in De-MIL-88B(Fe)-1.25/light/PDS system. In addition, the  $^1\text{O}_2$  via the transform of  $\bullet\text{OH}$  offered a minor contribution toward BPA degradation. Ultra-low PDS consumption resulted from the regeneration of  $\text{SO}_4^{2-}$  (Eq. 6) and  $\text{S}_2\text{O}_8^{2-}$  (Eq. 7). Fig. S39 indicated that De-MIL-88B(Fe)-1.25/PDS/light system could still exhibit outstanding cyclic performance in the low dose peroxydisulfate. Significantly, both the total peroxydisulfate input (1.0 mM) and consumption (0.26 mM, including the possible adsorbed peroxydisulfate on the catalyst surface) during BPA degeneration were lower than those of most other types of catalysts reported previously (Fig. 5g), also exhibiting its outstanding practical application prospects.

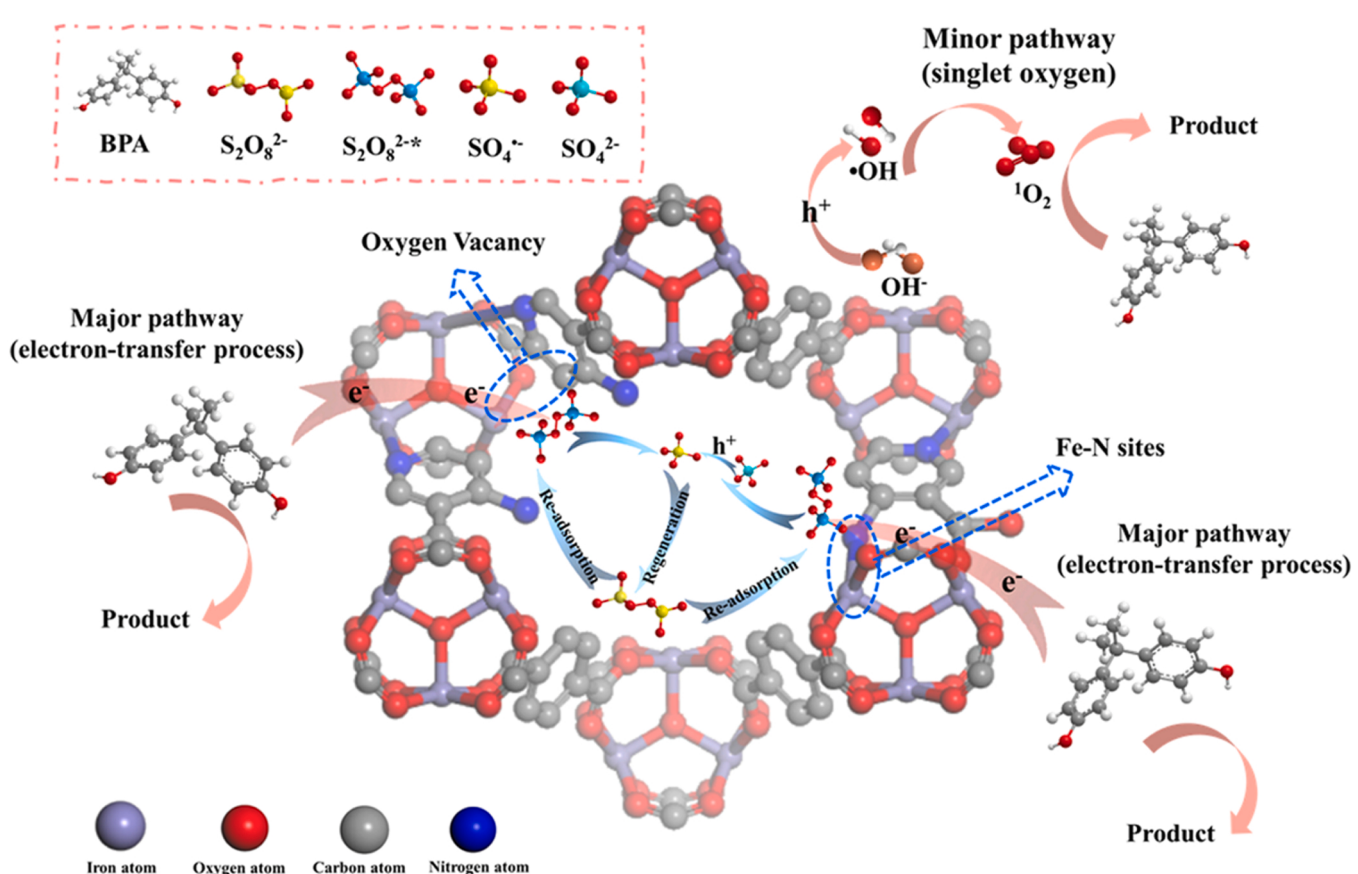


Fig. 6. The proposed mechanisms of BPA elimination in the De-MIL-88B(Fe)-1.25/light/PDS system.

#### 4. Conclusion

In all, series of defective MIL-88B(Fe) with rich nitrogen sites and oxygen vacancies were fabricated using 4-aminocitric acid as modulator, in which the optimal De-MIL-88B(Fe)-1.25 catalyst could persistently perform nonradical reaction with the aid of low concentration peroxydisulfate (1.0 mM) and visible light. De-MIL-88B(Fe)-1.25 with porous structure as well as abundant and uniform active Fe-N sites and oxygen vacancies facilitated peroxydisulfate adsorption and formed the surface-confined ROSs, achieving the transformation from ROSs reaction in MIL-88B(Fe) system to ETP in De-MIL-88B(Fe)-1.25 system. The generated sulfate during ETP could be oxidized to confined sulfate radicals in De-MIL-88B(Fe)-1.25, further inducing the regeneration of peroxydisulfate due to the self-quenching reaction, which were affirmed by series experiments and DFT calculations. Such reaction mechanism supported nearly 100% BPA elimination efficiency with ultra-low total peroxydisulfate consumption (0.26 mM, including the possible adsorbed peroxydisulfate on the catalyst surface) in five cycles. This work provided new insights into the rational design of persulfate-reaction-oriented catalyst and offered novel strategy to accomplish rapid and persistent decontamination of aqueous emerging pollutants with ultra-low consumption of chemicals like persulfate.

#### CRediT authorship contribution statement

**Yu-Hang Li:** Data curation, Investigation, Visualization, Writing – original draft. **Chong-Chen Wang:** Conceptualization, Funding acquisition, Supervision, Project administration, Writing – review & editing. **Fei Wang:** Investigation, Methodology, **Wen Liu:** Resources, Instrumental, **Long Chen:** Software, Methodology, **Chen Zhao:** Resources, Software. **Huifen Fu:** Resources, Software. **Peng Wang:** Resources, Instrumental, **Xiaoguang Duan:** Conceptualization, Supervision, Writing – review & editing.

#### Declaration of Competing Interest

The authors declare that they have no known competing financial interests or personal relationships that could have appeared to influence the work reported in this paper.

#### Data Availability

Data will be made available on request.

#### Acknowledgements

This work was supported by National Natural Science Foundation of China (22176012, 51878023), Beijing Natural Science Foundation (8202016), Science and Technology General Project of Beijing Municipal Education Commission (KM202110016010), and BUCEA Post Graduate Innovation Project (PG2022052).

#### Appendix A. Supporting information

Supplementary data associated with this article can be found in the online version at [doi:10.1016/j.apcatb.2023.122699](https://doi.org/10.1016/j.apcatb.2023.122699).

#### References

- [1] L.S. Zhang, X.H. Jiang, Z.A. Zhong, L. Tian, Q. Sun, Y.T. Cui, X. Lu, J.P. Zou, S. L. Luo, Carbon nitride supported high-loading Fe single-atom catalyst for activation of peroxymonosulfate to generate  ${}^1\text{O}_2$  with 100% selectivity, *Angew. Chem. Int. Ed. Engl.* 60 (2021) 21751–21755.
- [2] K. Qian, H. Chen, W. Li, Z. Ao, Y.N. Wu, X. Guan, Single-atom Fe catalyst outperforms its homogeneous counterpart for activating peroxymonosulfate to achieve effective degradation of organic contaminants, *Environ. Sci. Technol.* 55 (2021) 7034–7043.
- [3] Y.Y. Ahn, E.T. Yun, J.W. Seo, C. Lee, S.H. Kim, J.H. Kim, J. Lee, Activation of peroxymonosulfate by surface-loaded noble metal nanoparticles for oxidative degradation of organic compounds, *Environ. Sci. Technol.* 50 (2016) 10187–10197.
- [4] X. Mi, P. Wang, S. Xu, L. Su, H. Zhong, H. Wang, Y. Li, S. Zhan, Almost 100% Peroxymonosulfate Conversion to Singlet Oxygen on Single-atom  $\text{CoN}_{2+2}$  sites, *Angew. Chem. Int. Ed. Engl.* 60 (2021) 4588–4593.
- [5] S.H. Ho, Y.D. Chen, R. Li, C. Zhang, Y. Ge, G. Cao, M. Ma, X. Duan, S. Wang, N. Q. Ren, N-doped graphitic biochars from C-phycocyanin extracted Spirulina residue for catalytic persulfate activation toward nonradical disinfection and organic oxidation, *Water Res.* 159 (2019) 77–86.
- [6] C. Guan, J. Jiang, C. Luo, S. Pang, C. Jiang, J. Ma, Y. Jin, J. Li, Transformation of iodide by carbon nanotube activated peroxydisulfide and formation of iodoorganic compounds in the presence of natural organic matter, *Environ. Sci. Technol.* 51 (2017) 479–487.
- [7] P. Shao, J. Tian, F. Yang, X. Duan, S. Gao, W. Shi, X. Luo, F. Cui, S. Luo, S. Wang, Identification and regulation of active sites on nanodiamonds: establishing a highly efficient catalytic system for oxidation of organic contaminants, *Adv. Funct. Mater.* 28 (2018) 1705295.
- [8] W. Ren, G. Nie, P. Zhou, H. Zhang, X. Duan, S. Wang, The intrinsic nature of persulfate activation and N-doping in carbocatalysis, *Environ. Sci. Technol.* 54 (2020) 6438–6447.
- [9] G. Liu, S. You, Y. Tan, N. Ren, In situ photochemical activation of sulfate for enhanced degradation of organic pollutants in water, *Environ. Sci. Technol.* 51 (2017) 2339–2346.
- [10] N. Liu, N. Lu, H. Yu, S. Chen, X. Quan, Enhanced degradation of organic water pollutants by photocatalytic in-situ activation of sulfate based on Z-scheme  $\text{g-C}_3\text{N}_4/\text{BiPO}_4$ , *Chem. Eng. J.* 428 (2022), 132116.
- [11] H.C. Zhou, J.R. Long, O.M. Yaghi, Introduction to metal-organic frameworks, *Chem. Rev.* 112 (2012) 673–674.
- [12] B. Li, H.M. Wen, Y. Cui, W. Zhou, G. Qian, B. Chen, Emerging multifunctional metal-organic framework materials, *Adv. Mater.* 28 (2016) 8819–8860.
- [13] Y.C. Hao, L.W. Chen, J. Li, Y. Guo, X. Su, M. Shu, Q. Zhang, W.Y. Gao, S. Li, Z.L. Yu, L. Gu, X. Feng, A.X. Yin, R. Si, Y.W. Zhang, B. Wang, C.H. Yan, Metal-organic framework membranes with single-atomic centers for photocatalytic  $\text{CO}_2$  and  $\text{O}_2$  reduction, *Nat. Commun.* 12 (2021) 2682.
- [14] W. Pei, J. Zhang, H. Tong, M. Ding, F. Shi, R. Wang, Y. Huo, H. Li, Removal and reutilization of metal ions on ZIF-67/GO membrane via synergistic photocatalytic-photothermal route, *Appl. Catal. B* 282 (2021), 119575.
- [15] Y.-H. Li, P. Wang, C.-C. Wang, L. Y.B, State-of-the-art review of defective metal-organic frameworks for pollutant removal from water, *Chin. J. Inorg. Chem.* 38 (2022) 2342–2362.
- [16] Y.-H. Li, M.-Y. Liu, Y.-W. Wei, C.-C. Wang, P. Wang, Adsorption and photocatalytic desorption toward Cr(VI) over defect-induced hierarchically porous  $\text{UiO-66-(OH)_2}$ : a sustainable approach, *Environ. Sci. Nano* 10 (2023) 672–682.
- [17] X. Duan, H. Sun, Y. Wang, J. Kang, S. Wang, N-doping-induced nonradical reaction on single-walled carbon nanotubes for catalytic phenol oxidation, *ACS Catal.* 5 (2014) 553–559.
- [18] L. Liu, Q. Liu, Y. Wang, J. Huang, W. Wang, L. Duan, X. Yang, X. Yu, X. Han, N. Liu, Nonradical activation of peroxydisulfate promoted by oxygen vacancy-laden  $\text{NiO}$  for catalytic phenol oxidative polymerization, *Appl. Catal., B* 254 (2019) 166–173.
- [19] W. Ren, C. Cheng, P. Shao, X. Luo, H. Zhang, S. Wang, X. Duan, Origins of electron-transfer regime in persulfate-based nonradical oxidation processes, *Environ. Sci. Technol.* 56 (2022) 78–97.
- [20] S. Zhang, Y. Zhuo, C.I. Ezugwu, C.C. Wang, C. Li, S. Liu, Synergetic molecular oxygen activation and catalytic oxidation of formaldehyde over defective MIL-88B (Fe) nanorods at room temperature, *Environ. Sci. Technol.* 55 (2021) 8341–8350.
- [21] L. Dai, J. Xu, J. Lin, L. Wu, H. Cai, J. Zou, J. Ma, Iodometric spectrophotometric determination of peroxydisulfate in hydroxylamine-involved AOPs: 15 min or 15 s for oxidative coloration? *Chemosphere* 272 (2021), 128577.
- [22] C. Liang, C.F. Huang, N. Mohanty, R.M. Kurakalva, A rapid spectrophotometric determination of persulfate anion in ISCO, *Chemosphere* 73 (2008) 1540–1543.
- [23] N. Liu, J. Wu, F. Fei, J. Lei, W. Shi, G. Quan, S. Zeng, X. Zhang, L. Tang, Ibuprofen degradation by a synergism of facet-controlled MIL-88B(Fe) and persulfate under simulated visible light, *J. Colloid Interface Sci.* 612 (2022) 1–12.
- [24] Marian Koman, Milan Melnik, J. Moncol, Crystal and molecular structure of copper (II) (pyridine-2,6-dicarboxylato)(2,6-dimethanolpyridine), *Inorg. Chem. Commun.* 3 (2000) 262–266.
- [25] J. Tang, J. Wang, Metal organic framework with coordinatively unsaturated sites as efficient fenton-like catalyst for enhanced degradation of sulfamethazine, *Environ. Sci. Technol.* 52 (2018) 5367–5377.
- [26] Y. Gao, T. Wu, C. Yang, C. Ma, Z. Zhao, Z. Wu, S. Cao, W. Geng, Y. Wang, Y. Yao, Y. Zhang, C. Cheng, Activity trends and mechanisms in peroxymonosulfate-assisted catalytic production of singlet oxygen over atomic metal-N-C catalysts, *Angew. Chem. Int. Ed. Engl.* 60 (2021) 22513–22521.
- [27] Y.-H. Li, C.-C. Wang, X. Zeng, X.-Z. Sun, C. Zhao, H. Fu, P. Wang, Seignette salt induced defects in Zr-MOFs for boosted Pb(II) adsorption: universal strategy and mechanism insight, *Chem. Eng. J.* 442 (2022), 136276.
- [28] X. Liao, F. Wang, F. Wang, Y. Cai, Y. Yao, B.-T. Teng, Q. Hao, L. Shuxiang, Synthesis of (100) surface oriented MIL-88A-Fe with rod-like structure and its enhanced fenton-like performance for phenol removal, *Appl. Catal. B* 259 (2019), 118064.
- [29] K. Zhao, Z. Zhang, Y. Feng, S. Lin, H. Li, X. Gao, Surface oxygen vacancy modified  $\text{Bi}_2\text{MoO}_6/\text{MIL-88B(Fe)}$  heterostructure with enhanced spatial charge separation at the bulk & interface, *Appl. Catal. B* 268 (2020), 118740.

[30] Y.-H. Li, X.-H. Yi, Y.-X. Li, C.-C. Wang, P. Wang, C. Zhao, W. Zheng, Robust Cr(VI) reduction over hydroxyl modified  $\text{UiO-66}$  photocatalyst constructed from mixed ligands: Performances and mechanism insight with or without tartaric acid, *Environ. Res.* 201 (2021), 111596.

[31] G. Yang, H. Yin, W. Liu, Y. Yang, Q. Zou, L. Luo, H. Li, Y. Huo, H. Li, Synergistic Ag/TiO<sub>2</sub>-N photocatalytic system and its enhanced antibacterial activity towards *Acinetobacter baumannii*, *Appl. Catal. B* 224 (2018) 175–182.

[32] B. Wang, C. Cheng, M. Jin, J. He, H. Zhang, W. Ren, J. Li, D. Wang, Y. Li, A site distance effect induced by reactant molecule matchup in single-atom catalysts for fenton-like reactions, *Angew. Chem. Int. Ed. Engl.* (2022), e202207268.

[33] Y. Yao, C. Wang, X. Yan, H. Zhang, C. Xiao, J. Qi, Z. Zhu, Y. Zhou, X. Sun, X. Duan, J. Li, Rational regulation of Co-N-C coordination for high-efficiency generation of  $^1\text{O}_2$  toward nearly 100% selective degradation of organic pollutants, *Environ. Sci. Technol.* 56 (2022) 8833–8843.

[34] Y. Bu, H. Li, W. Yu, Y. Pan, L. Li, Y. Wang, L. Pu, J. Ding, G. Gao, B. Pan, Peroxydisulfate activation and singlet oxygen generation by oxygen vacancy for degradation of contaminants, *Environ. Sci. Technol.* 55 (2021) 2110–2120.

[35] D. Tan, F. Huang, S. Guo, D. Li, Y. Yan, W. Zhang, Efficient photocatalytic tetracycline elimination over Z-scheme g-C<sub>3</sub>N<sub>4</sub>/Bi<sub>2</sub>O<sub>3</sub> heterojunction under sunshine light: Performance, mechanism, DFT calculation and pathway, *J. Alloy. Compd.* 946 (2023), 169468.

[36] F.-X. Wang, C.-C. Wang, X. Du, Y. Li, F. Wang, P. Wang, Efficient removal of emerging organic contaminants via photo-Fenton process over micron-sized Fe-MOF sheet, *Chem. Eng. J.* 429 (2022), 132495.

[37] W. Wang, Y. Liu, Y. Yue, H. Wang, G. Cheng, C. Gao, C. Chen, Y. Ai, Z. Chen, X. Wang, The confined interlayer growth of ultrathin two-dimensional Fe<sub>3</sub>O<sub>4</sub> nanosheets with enriched oxygen vacancies for peroxymonosulfate activation, *ACS Catal.* 11 (2021) 11256–11265.

[38] C. Zhao, Z. Wang, X. Li, X.-H. Yi, H. Chu, X. Chen, C.-C. Wang, Facile fabrication of BUC-21/Bi<sub>2</sub>O<sub>3</sub>Br<sub>10</sub> composites for enhanced photocatalytic Cr(VI) reduction under white light, *Chem. Eng. J.* 389 (2020), 123431.

[39] L. Chen, J. Duan, P. Du, W. Sun, B. Lai, W. Liu, Accurate identification of radicals by in-situ electron paramagnetic resonance in ultraviolet-based homogenous advanced oxidation processes, *Water Res.* 221 (2022), 118747.

[40] C. Luo, J. Ma, J. Jiang, Y. Liu, Y. Song, Y. Yang, Y. Guan, D. Wu, Simulation and comparative study on the oxidation kinetics of atrazine by UV/H<sub>2</sub>O<sub>2</sub>, UV/HSO<sub>5</sub> and UV/S<sub>2</sub>O<sub>8</sub><sup>2-</sup>, *Water Res.* 80 (2015) 99–108.

[41] X.-W. Zhang, F. Wang, C.-C. Wang, P. Wang, Hf Fu, C. Zhao, Photocatalysis activation of peroxydisulfate over the supported Fe<sub>3</sub>O<sub>4</sub> catalyst derived from MIL-88A(Fe) for efficient tetracycline hydrochloride degradation, *Chem. Eng. J.* 426 (2021), 131927.

[42] A. Du, H. Fu, P. Wang, C. Zhao, C.C. Wang, Enhanced catalytic peroxymonosulfate activation for sulfonamide antibiotics degradation over the supported CoS<sub>x</sub>-CuS<sub>x</sub> derived from ZIF-L(Co) immobilized on copper foam, *J. Hazard. Mater.* 426 (2022), 128134.

[43] C. Zhao, L. Meng, H. Chu, J.-F. Wang, T. Wang, Y. Ma, C.-C. Wang, Ultrafast degradation of emerging organic pollutants via activation of peroxymonosulfate over Fe<sub>3</sub>C/Fe@N-C-x: Singlet oxygen evolution and electron-transfer mechanisms, *Appl. Catal. B* 321 (2023), 122034.

[44] Y. Zong, H. Zhang, X. Zhang, W. Liu, L. Xu, D. Wu, High-valent cobalt-oxo species triggers hydroxyl radical for collaborative environmental decontamination, *Appl. Catal. B* 300 (2022), 120722.

[45] S. Zhu, X. Li, J. Kang, X. Duan, S. Wang, Persulfate activation on crystallographic manganese oxides: mechanism of singlet oxygen evolution for nonradical selective degradation of aqueous contaminants, *Environ. Sci. Technol.* 53 (2019) 307–315.

[46] J. Chen, X. Zhou, P. Sun, Y. Zhang, C.H. Huang, Complexation enhances Cu(II)-activated peroxydisulfate: a novel activation mechanism and Cu(III) contribution, *Environ. Sci. Technol.* 53 (2019) 11774–11782.

[47] Q. Yang, Y. Chen, X. Duan, S. Zhou, Y. Niu, H. Sun, L. Zhi, S. Wang, Unzipping carbon nanotubes to nanoribbons for revealing the mechanism of nonradical oxidation by carbocatalysis, *Appl. Catal., B* 276 (2020), 119146.

[48] Y. Chen, G. Zhang, H. Liu, J. Qu, Confining free radicals in close vicinity to contaminants enables ultrafast fenton-like processes in the interspacing of MoS<sub>2</sub> membranes, *Angew. Chem. Int. Ed. Engl.* 58 (2019) 8134–8138.

[49] Y. Yang, P. Zhang, K. Hu, P. Zhou, Y. Wang, A.H. Asif, X. Duan, H. Sun, S. Wang, Crystallinity and valence states of manganese oxides in Fenton-like polymerization of phenolic pollutants for carbon recycling against degradation, *Appl. Catal., B* 315 (2022), 121593.

[50] Z. Wei, M. Liu, Z. Zhang, W. Yao, H. Tan, Y. Zhu, Efficient visible-light-driven selective oxygen reduction to hydrogen peroxide by oxygen-enriched graphitic carbon nitride polymers, *Energy Environ. Sci.* 11 (2018) 2581–2589.

[51] X. Zhang, P. Ma, C. Wang, L. Gan, X. Chen, P. Zhang, Y. Wang, H. Li, L. Wang, X. Zhou, K. Zheng, Unraveling the dual defect sites in graphite carbon nitride for ultra-high photocatalytic H<sub>2</sub>O<sub>2</sub> evolution, *Energy Environ. Sci.* 15 (2022) 830–842.

[52] W. Ren, L. Xiong, X. Yuan, Z. Yu, H. Zhang, X. Duan, S. Wang, Activation of peroxydisulfate on carbon nanotubes: electron-transfer mechanism, *Environ. Sci. Technol.* 53 (2019) 14595–14603.

[53] M. Li, S. You, X. Duan, Y. Liu, Selective formation of reactive oxygen species in peroxymonosulfate activation by metal-organic framework-derived membranes: a defect engineering-dependent study, *Appl. Catal. B* 312 (2022), 121419.

[54] Y. Gong, B. Yang, H. Zhang, X. Zhao, A g-C<sub>3</sub>N<sub>4</sub>/MIL-101(Fe) heterostructure composite for highly efficient BPA degradation with persulfate under visible light irradiation, *J. Mater. Chem. A* 6 (2018) 23703–23711.

[55] W.-D. Oh, Z. Wong, X. Chen, K.-Y.A. Lin, A. Veksha, G. Lisak, C. He, T.-T. Lim, Enhanced activation of peroxydisulfate by CuO decorated on hexagonal boron nitride for bisphenol A removal, *Chem. Eng. J.* 393 (2020), 124714.